Materials & Design 221 (2022) 110968

Contents lists available at ScienceDirect

Materials & Design

journal homepage: www.elsevier.com/locate/matdes

All laser-based fabrication of microchannel heat sink

Haoyu Zhou [a], Jungbae Lee [b], Minsoo Kang [a], Hakgae Kim [a,b], Hyoungsoon Lee [a,c,*], Jung Bin In [a,b,*]

[a] Department of Intelligent Energy and Industry, Chung-Ang University, Seoul 06974, Republic of Korea
[b] Soft Energy Systems and Laser Applications Laboratory, School of Mechanical Engineering, Chung-Ang University, Seoul 06974, Republic of Korea
[c] Advanced Thermal Systems Laboratory, School of Mechanical Engineering, Chung-Ang University, Seoul 06974, Republic of Korea

HIGHLIGHTS

- Rapid all laser-based fabrication of silicon microchannel device.
- Laser engraving of microchannels, laser drilling of inlet/outlet holes, laser sintering of film heater, and laser welding for packaging.
- Application in microchannel heat sink for miniaturized devices.

GRAPHICAL ABSTRACT

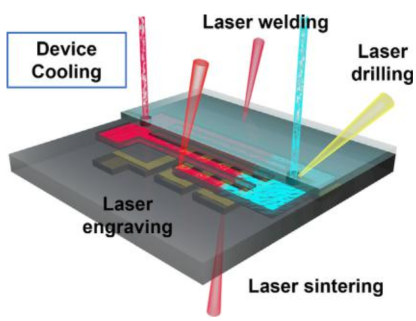

ARTICLE INFO

Article history:
Received 14 April 2022
Revised 10 July 2022
Accepted 19 July 2022
Available online 22 July 2022

Keywords:
Microchannel heat sink
Laser processing
Flow boiling heat transfer
Laser machining

ABSTRACT

Microchannel heat sinks have been recognized as efficient cooling platforms for thermal management of miniaturized devices because of their compact structure. Unlike most microfabrication processes, laser micromachining is a versatile direct writing method to rapidly produce microchannels in brittle substrates such as silicon wafers. In this study, an all-laser fabrication method is proposed to fabricate a microfluidic heat sink for silicon devices. Lasers are used for engraving microchannels on a silicon wafer, drilling inlet/outlet holes in quartz glass cover, and welding the Si sample and quartz glass cover. The entire fabrication process is completed within two hours. The microchannel surface is converted into a hydrophilic wall as proven by contact angle measurement, and a water flow is easily introduced to the channel as a cooling fluid. The boiling heat transfer performance of the fabricated microfluidic channel is evaluated by applying heat to the bottom of the device. A micro-heater placed underneath the Si substrate is also prepared using a laser to induce selective sintering of a conductive Ag layer. The heat generated by the heater is successfully removed by boiling heat transfer, and the critical heat flux is measured to be ~ 55.2 W/cm^2 at a water flux of 208 kg/m^2s.

1. Introduction

In the era of 5th generation mobile networks (5G) and artificial intelligence (AI), continuous improvement of data processing and communication speeds, and the constant reduction in component sizes have led to an increase in the power density of electronic products. As a result, the thermal management of electronic circuits and devices has become the main challenge for future electronics. Among various forms of heat removal techniques, microchannel heat sinks have been widely recognized as an efficient cooling platform for various applications, such as high-performance processors, solar cells, fuel cells, and other high-heat-flux devices [1–3]. Flow boiling heat transfer occurring in microchannels has been extensively studied for its higher heat flux,

* Corresponding authors at: Department of Intelligent Energy and Industry, Chung-Ang University, Seoul 06974, Republic of Korea.
E-mail addresses: leeh@cau.ac.kr (H. Lee), jbin@cau.ac.kr (J.B. In).

https://doi.org/10.1016/j.matdes.2022.110968
0264-1275/

lower pump power, and higher efficiency [4,5]. Microchannel heat sinks are highly suitable for modern miniaturized devices because of their large heat transfer area, compact structure, and uniform wall temperature distribution [6,7]. Therefore, it is imperative to develop a novel manufacturing method for producing microchannel heat sinks in a facile way at reduced costs.

Various microfabrication techniques have been developed to produce microfluidic channels in Si and quartz glass materials. Si is a representative material widely used in semiconductor devices and other microdevices, and quartz glass is a popular substrate owing to its optical transparency, chemical stability, biocompatibility, high-temperature resistance, and minimal thermal expansion. Microfabrication techniques based on micro-scale photolithography, deposition, and etching are commonly used for fabricating microchannels [8–10]. For example, deep reactive ion etching (DRIE) has been adopted to especially produce deep microchannels in a Si wafer [11,12]. However, these microfabrication processes are time-consuming, complicated, require expensive micropattern mask and processing equipment, and produce chemical pollutants [13,14]. Moreover, they should be carried out in a clean room environment, further raising the fabrication cost.

Mechanical machining based on micro-cutting/milling using computer numerical control (CNC) can also be a simple and rapid process for producing microfluidic patterns [15–17]. However, the cutting tool and the debris generated during the machining process often cause high stress in a local part of the workpiece, resulting in fractures of brittle materials such as Si and glass. In addition, the degree of tool wear is difficult to monitor, and other inspection methods for wear detection, such as laser tool measurement or tool-workpiece voltage monitoring, should be adopted for reliable processing [18]. Moreover, the end mill for micro-milling should be carefully designed differently from the tool geometry for macro-milling, thus increasing fabrication costs [19,20].

Compared with the above-mentioned fabrication methods, laser micromachining is a versatile machining technique that can produce microchannels in a facile way. Laser processing is generally not limited by the mechanical properties of the workpiece as a wide range of materials, including brittle Si and glass, can be reliably cut using a laser. In addition, various microscale features can be rapidly engraved on materials via a programmed laser scanning path without requiring pattern masking. Moreover, laser micromachining is a non-contact method free of tool wear monitoring, and the instantaneous laser ablation does not generally require tight control of ambient gas conditions.

Recently, numerous studies have been conducted on laser micromachining for fabricating microchannels in Si wafers [21–26]. While expensive femtosecond (fs) lasers—the most representative ultrashort laser—enable high-resolution machining, relatively economical nanosecond (ns) lasers have been adopted for implementing laser-based micromachining of microchannels with tens of micrometers in size. Most of the previous studies focused on realizing micromachining of Si with lasers and exploring various scientific or engineering aspects of the related laser ablation process. However, the laser-based fabrication of microchannel is only a part of the entire processes to build a functional microfluidic device, whereas efficient laser processing can be widely applied to the other fabrication processes for further improving the fabrication efficiency.

In this study, an all-laser microfabrication technique was developed by integrating various laser-based maskless fabrication techniques for rapidly fabricating a microchannel heat sink in a Si device. Laser-engraved microchannels have been studied for various applications as found in the related literature [24,25]. However, according to our research, this device-level rapid fabrication based on all-laser microfabrication, especially for the application in flow boiling heat transfer, has rarely been reported. Our all-laser fabrication method included the following processes: hydrophilic microchannels were produced in a Si wafer by using a ns laser; an on-chip micro-heater was patterned on the other side of the Si sample via laser-induced sintering of Ag nanoparticles; inlet/outlet holes were drilled in a quartz glass plate, later adopted as a transparent cover for packaging. Moreover, bonding between the Si sample and quartz glass cover was achieved via laser transmission welding. While conventional anodic bonding requires relatively high process temperatures (up to ~ 450 °C) under high voltages, which can be detrimental to the functionality of the device [27–29], laser welding enabled tight bonding with a minimal thermal budget. Finally, the performance of the fabricated microchannel heat sink was evaluated based on critical heat flux (CHF), pressure drop, and wall temperature at different mass fluxes.

2. Experimental section

2.1. Materials

The microfluidic device was fabricated on a Si wafer (p-type, double side polished, orientation ⟨1 0 0⟩, thickness: ~525 μm, resistivity: 1–20 Ω·cm). A quartz glass (or fused silica) plate (size: 25×25 mm^2, thickness: 1 mm) was used as a transparent cover for the device. For the fabrication of on-chip heater unit beneath the device, a dispersion of Ag nanoparticles (AgNPs, 10 wt% in isopropyl alcohol, avg. diameter: 50 nm, SNP-050c, Flexio CO.) and a poly (pyromellitic dianhydride-*co*-4,40-oxydianiline) amic acid (PAA; 12.8 wt% in 80 % *N*-Methyl-2-pyrrolidone and 20 % aromatic hydrocarbon; Sigma-Aldrich) were used.

2.2. Laser micromachining and welding

For cutting a Si wafer, engraving microchannels, and welding Si and quartz glass cover, a nanosecond (ns) pulsed fiber laser (pulse duration: ~250 ns, wavelength: 1062 nm, SP-050P-A-EP- Z-B-Y, SPI Co.) was used. The laser beam was directed onto the sample plane using a 2-axis galvanometer scanner (DCB210-Y1HP, Thorlabs). The output laser beam was focused via an F-theta lens (focal length: 163 mm, SL16385-Y1, Thorlabs), and the size of the focused laser beam was ~63 μm. The laser scanning path was automatically programmed based on pattern geometry and dimensions through scanner software (SAMLight, SCAPS GmbH). This system enabled rapid direct writing of micropatterns. For example, when the scanning speed and line-to-line distance (pitch) were set to 500 mm/s and 50 μm, respectively, the entire engraving of microchannels only took ~ 5.5 *sec* per device. For laser drilling into the quartz glass cover, a CO_2 laser (wavelength: 10.6 μm, beam diameter: ~260 μm, C40–50, Coryart Co.) was adopted. For all laser processing, the laser power output was directly measured by using a laser power meter (Nova II Ophir Co.).

2.3. Fabrication of on-chip heater

For fabricating the on-chip heater, the backside of the device wafer was coated with PAA using a spin coater (SPIN-1200D, MIDAS Co.) at 1000 RPM for 20 s, 1500 RPM for 30 s, and 500 RPM for 20 s. The PAA film was dried in a vacuum oven (HQ-VDO27, CORETECH) at 100 °C for 1 h. The dried film was additionally annealed on a hot plate (HP-180D, MTOPS) at 250 °C for ~ 30 min, being imidized into polyimide (PI). The PI film on Si was then coated with AgNPs by applying the AgNP dispersion on it and immediately spinning the wet sample at 300 RPM for 60 s. The sample was subsequently dried in a convection oven (SH-DO-90FH, Samheung Co.) at 50 °C for 5 mins. The same fiber laser unit also enabled operation in a continuous wave (CW) mode, producing a CW laser beam of the same wavelength (1062 nm). This CW laser beam was adopted for sintering the coated AgNPs. A patterned area of the AgNP layer was selectively irradiated by programmed scanning of the CW laser beam (power: 4.8 W, scanning speed: 300 mm/s, number of scans: 2), and the AgNPs on the irradiated area were consequently sintered by the laser-induced heat. The unaffected area of the AgNP layer was then selectively washed out by rinsing the sample in deionized (DI) water, leaving a conductive Ag heater pattern on PI [30–32].

2.4. Characterizations

A scanning electron microscope (SEM, S-3400 N, Hitachi) system and an optical microscope were used to observe the surface structure of the Si samples and measure the dimensions of the microchannels. The morphology of Ag nanoparticles was observed by field emission scanning electron microscopy (FE-SEM) (SIGMA, Carl Zeiss AG). X-ray photoelectron spectroscopy (XPS, K-alpha +, Thermo Fisher Scientific) was used to analyze the elemental composition of the Si wafer surface after laser ablation. The pass energy for the survey scan was set to 200 eV, and the step size was adjusted to 1.0 eV.

3. Results and discussion

3.1. All-laser fabrication of microchannels

A microchannel heat sink, comprising a Si substrate with a microchannel and micro-heater, a transparent cover, and tube fitting connectors, was fabricated based on laser processing. Fig. 1 describes the all-laser fabrication processes. A Si wafer was precisely diced into a device piece, and microchannels were engraved on it via programmed laser scanning. A transparent quartz glass cover punctured for inlet/outlet ports was attached to the Si piece via laser welding. The bottom surface of the Si piece was then coated with AgNPs, which were subsequently sintered into a micro-heater by the laser. The inlet/outlet ports were finally connected to tubing for introducing a fluid flow. Different lasers were applied to the fabrication processes due to dissimilar light-material interaction characteristics of the target materials. Laser processing parameters were also adjusted depending on the desired depth of machining and processing temperature. The details of the fabrication process are discussed below.

3.1.1. Laser cutting of Si wafers and channel engraving

Laser cutting and engraving of a Si wafer were implemented based on ns laser ablation. The ns fiber laser was used for this purpose. The laser pulse duration and pulse repetition frequency (PRF) were 250 ns and 50 kHz, respectively. For exploring the effects of laser fluence, scanning speed, and the number of scans on the dimensions of ablated groove, a parametric study was performed by varying these parameters (Figure S1 of Supplementary Material), and based on its result, the laser irradiation parameters were determined for cutting and engraving the Si wafer.

A Si wafer was cut into a square piece (size: 3 cm × 3 cm) using the ns fiber laser at a laser fluence of 33.1 J/cm^2, a scanning speed of 500 mm/s, and a scanning number of 10. The entire pattern area, including microchannels and reservoir parts, was 1 cm × 2 cm. The pattern shape and its dimensions are described in Figure S2. Forty parallel microchannels were engraved in the pattern by raster-scanning the Si surface with the ns fiber laser at a laser fluence of 30 J/cm^2, a scanning speed of 500 mm/s, and a line-to-line spacing of 50 μm. This laser scanning was repeated 3 times along the same path to deepen the channel. The size of each microchannel was approximately 1 cm × 0.12 mm × 0.08 mm (length × width × depth). After engraving, the top surface of the Si sample was flattened using a polishing machine (Labopol-5, Struers Co.) with sandpaper of particle size 2.5 μm (Si carbide 1200/4000, R&B lnc Co.) at 300 rpm for 5 min to remove the recast layer and particles generated by laser ablation from the top surface. Fig. 2a and b show the cross-sectional SEM view of the

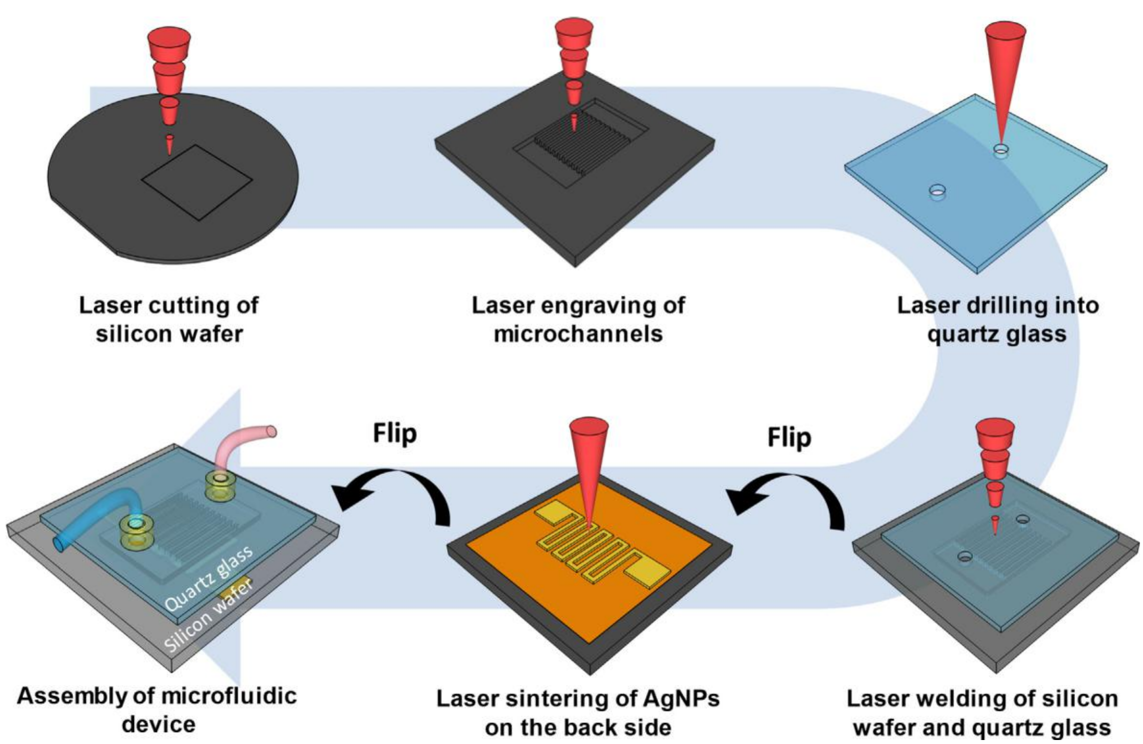

Fig. 1. Process diagram for all-laser fabrication of microchannel heat sink device.

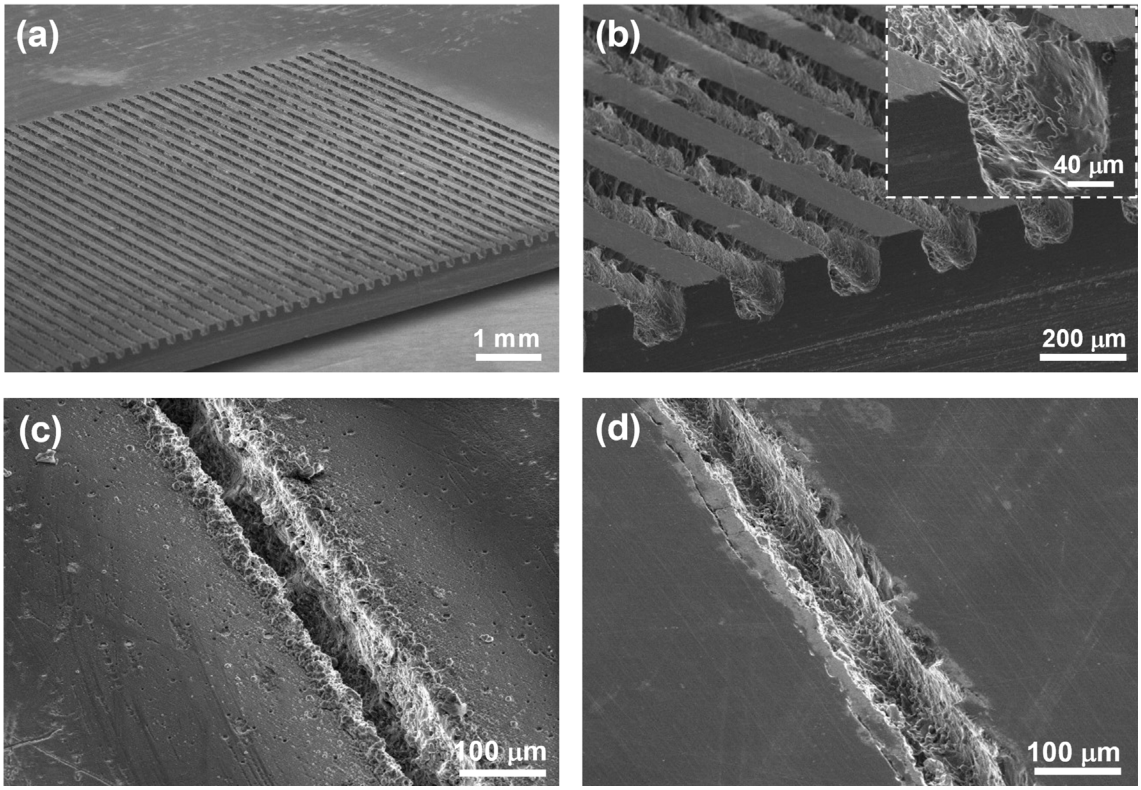

Fig. 2. SEM images of laser-engraved microchannels: (a) cross-sectional image of Si microchannels obtained at an oblique angle and (b) magnified images captured at the same angle, and top view images of a single microchannel obtained at an oblique angle (c) before and (d) after polishing.

produced microchannels. The average roughness (Ra) of the polished surface was measured to be 4.21 nm by atomic force microscopy (AFM, XE-100, PSIA) (figure S3). The effect of polishing is elucidated by comparing the surface morphologies of a single microchannel obtained before and after polishing (Fig. 2c and d, respectively).

In laser engraving, laser ablation influences temperature distribution in the Si wafer *via* heat conduction, whereas the heat is locally generated primarily near the beam spot. In the microchannel heat sink, the functional device is supposed to be placed on the other side of the Si substrate; when laser engraving is performed after the device fabrication, its operation can be affected by the heat induced in the microchannel engraving process. Thus, the thermal effect of laser engraving on the temperature distribution of the Si wafer was investigated.

The temperature change induced by laser engraving was measured at the center point of the bottom surface using a thermocouple (K type), as described in the inset of Fig. 3a. A nitrogen flow was introduced onto the engraving area during the microchannel engraving process at a flow rate of ~ 8 l/min to investigate its effect on the Si temperature. The plot in Fig. 3a shows the result, revealing that the temperature quite moderately rose to ~ 131 °C during the engraving process with nitrogen blowing. The change in engraving depth by nitrogen blowing was almost negligible. The internal temperature of the irradiated Si wafer was further investigated using a commercial finite element method (FEM) software (COMSOL Multiphysics) [33–35]. The temperature distribution in the Si wafer was calculated based on a simplified 2D model. Fig. 3b shows the temperature distribution and isotherms captured at ~ 1.6 msec after laser engraving was initiated. The distance from the beam spot to the 250 °C isotherm was estimated to be roughly 100 μm. The details of the simulation are explained in the supporting information.

The laser irradiation of Si wafer remarkably enhanced the water wettability of the engraved Si channels (see water wicking in supplementary video V1). To investigate the wettability change, a Si sample was prepared by scanning its surface in a square area (size: 2×2 cm^2) with the ns fiber laser using the same laser engraving parameters as those of the above channel engraving. A water droplet (vol: 5 μl) was dropped onto the surface, and the contact angle was measured. While the contact angle of the water droplet was ~ 51° to the pristine Si wafer surface (Fig. 4a), the contact angle of the droplet for the laser-irradiated Si surface was almost 0°, confirming the complete wetting and excellent hydrophilicity of the laser-irradiated Si surface (Fig. 4b).

The surface morphology and compositional characteristics of the irradiated surface were further investigated by SEM and XPS. Fig. 4c shows a high-magnification SEM image of the irradiated surface, revealing a rough and porous surface structure with a capillary network. The surface roughness was measured to be ~ 6.75 μm (Figure S5). Fig. 4d shows an XPS survey spectrum of the irradiated surface. The distinct peak corresponding to O1s suggests the generation of Si oxide, which is attributed to ns laser ablation in air [36]. The high-resolution XPS spectrum of Si 2p (Fig. 4e) reveals a dominant peak of SiO_2, confirming the oxidization of the ablated Si surface.

The surface structure of these physical and chemical characteristics is widely known to favor efficient boiling heat transfer performance [37]. Considering the nucleate boiling heat transfer, this structure features more nucleation sites, smaller departure bubbles, and higher departure frequency relative to a smooth surface [38,39]. Si oxide is a representative hydrophilic material with great affinity to water droplets, and the roughness increase further enhances wetting of the oxidized surface [36]. As a result, the laser-irradiated surface exhibited superhydrophilicity, which facilitates quick water replenishment in the partially dry-out area during boiling [40].

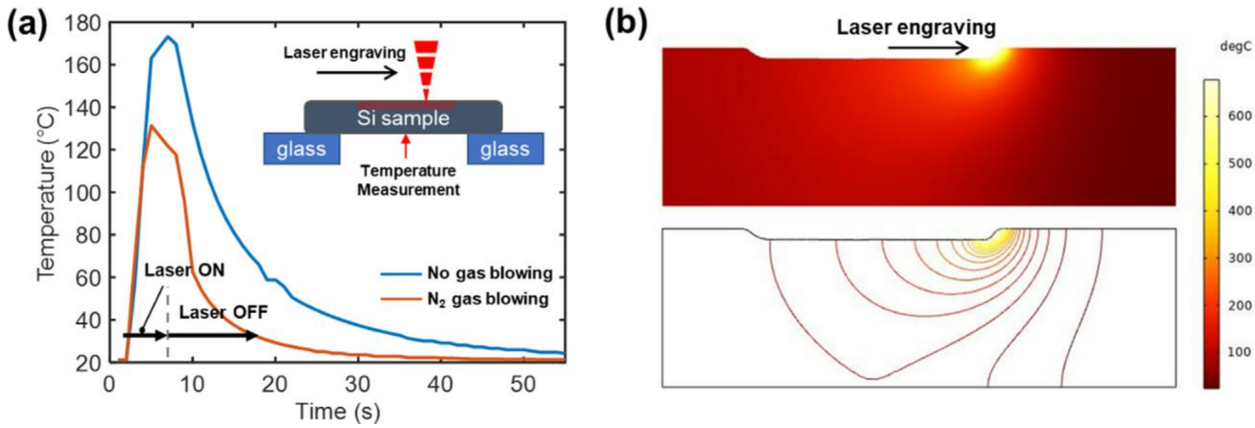

Fig. 3. (a) Temperature measured at the bottom center of the Si sample for the period of laser engraving and after the termination of laser irradiation. (b) Temperature distribution (color map and isotherms) calculated based on FEM simulation. This time step was selected to facilitate visualization of temperature distribution, whereas the maximum temperature at the beam spot was significantly higher than the value shown in the figure.

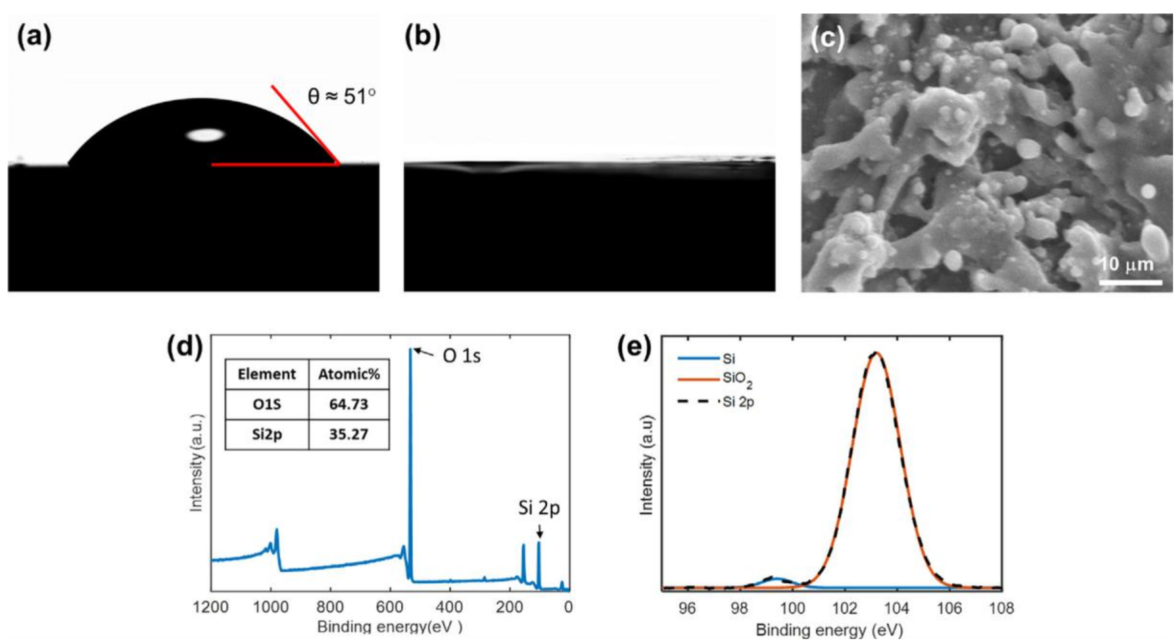

Element	Atomic%
O1S	64.73
Si2p	35.27

Fig. 4. Images of contact angle (a) before and (b) after laser ablation of the Si wafer. (c) SEM image of the capillary structure of the laser-ablated Si surface. (d) XPS survey spectrum and (e) high-resolution Si 2p spectrum of the laser-ablated Si surface.

3.1.2. Laser drilling through quartz glass cover

A transparent cover was prepared from a quartz glass plate. Inlet and outlet through-holes (diameter: ~1.3 mm) were drilled into the quartz glass plate using the CO_2 laser (wavelength: 10.6 μm). As the hole diameter is significantly larger than that of the incident laser beam, laser trepanning drilling, where the laser beam moves following a circular path, was adopted. The quartz glass plate was scanned 3 times with the laser beam at a laser power of 48 W (425 kW/cm^2 in power density) and a scanning speed of 10 mm/s. After drilling, the surface of the quartz glass plate was also polished (average roughness: 1.37 nm, figure S3) in the same way as the Si sample. Polishing of the Si sample and quartz glass cover was required to enhance the contact between the two plates for the subsequent laser welding. Fig. 5a shows a digital photograph of the quartz glass plate with laser-drilled holes and a magnified optical microscopy image of the through-hole.

3.1.3. Laser welding

The quartz glass cover and Si sample were assembled *via* laser transmission welding [41,42]. These plates were cleaned using an ethanol-soaked wiper and dried in a nitrogen flow before welding. The cover plate was placed on top of the Si sample with the hole positions relatively aligned with the microchannel pattern and was pressed down to achieve local optical contact. For laser transmission welding, the ns fiber laser was used. Using a CW fiber laser was not effective for welding because the continuous input of the laser beam induced excessive heat in the enlarged heat-affected area, immediately resulting in fractures in the cover plate.

Fig. 5b describes the laser welding process. The ns fiber laser beam was focused on the interface of the cover plate and Si sample. The laser beam was transmitted through the quartz glass cover, being absorbed in the interface. The welding area was set surrounding the engraved channels and irradiated with the laser beam along a raster-scanning path at a laser fluence of 11.9 J/

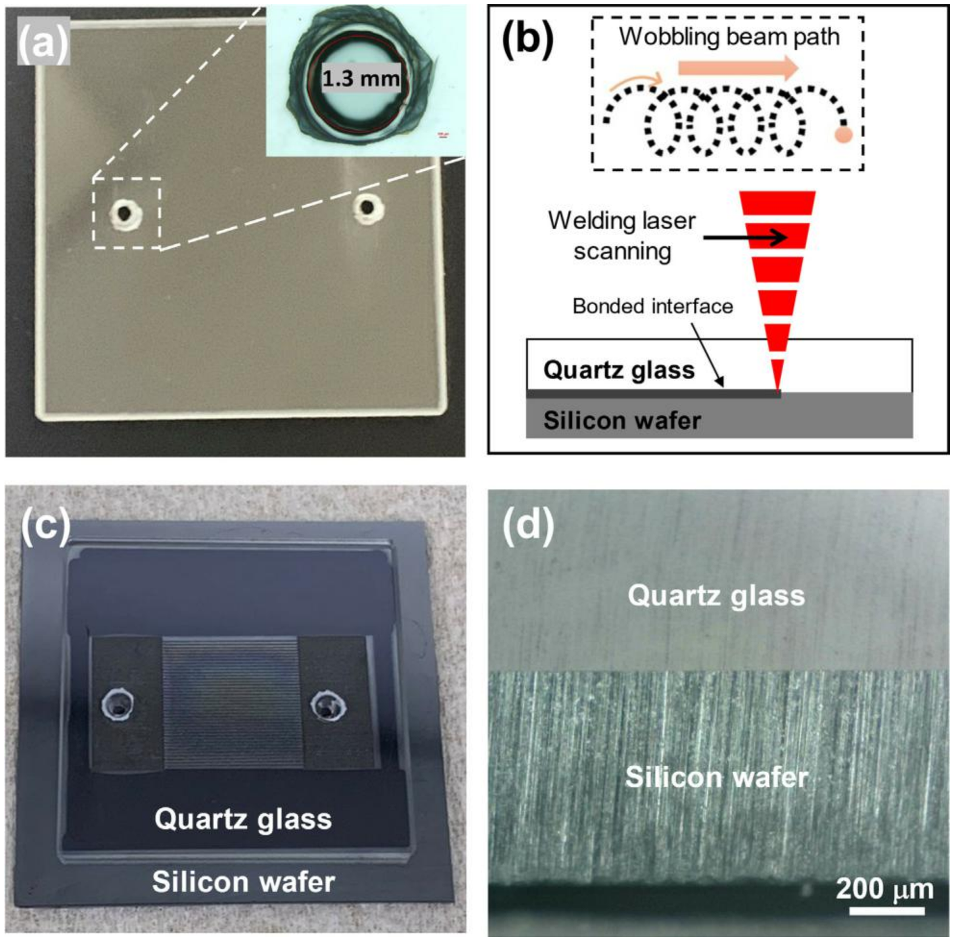

Fig. 5. (a) Digital photograph of quartz glass cover with two laser-drilled holes for inlet and outlet (inset: enlarged image of the hole). (b) Schematic description of laser transmission welding. (c) Digital photograph of laser-welded Si wafer and quartz glass cover. (d) Cross-sectional optical microscopy of laser-welded quartz glass and Si wafer.

cm^2, PRF of 1000 kHz, scanning speed of 5 mm/s, and line-to-line spacing of 0.5 mm. For improving the welding quality, wobbling of the laser beam was adopted at an amplitude of 0.5 mm and wobbling frequency of 100 Hz as described in the inset of Fig. 5b. Compared with the anodic bonding method conventionally used for Si wafer and glass, the processing time for this laser welding was significantly shortened, and high-quality welding was achieved within ~ 1 min. Moreover, heat was locally generated in the interface only, resulting in a minimal thermal budget (figure S6).

The welding quality was confirmed by pressurizing the internal channel space. Neither cracks in the device nor leakage of water was found until the pressure reached 4 bar, above which water started to leak out of the epoxy bonding area that connected the tube and the port of the cover. Fig. 5c shows a digital photograph of the welded quartz glass cover and Si sample. Fig. 5d and Figure S7 show its optical microscopy and SEM cross-sectional image, respectively, revealing tight bonding without any visible gaps.

3.1.4. Laser sintering of AgNPs

For investigating the boiling heat transfer performance of the laser engraved microchannel, an on-chip heater element was fabricated on the bottom surface of the Si sample. Joule heating of the Si sample was implemented by patterning a serpentine conductive film via laser-induced sintering of AgNPs [30,31]. Fig. 6a describes the laser-induced sintering process: when the coated AgNPs are irradiated with a laser, sintering of the irradiated AgNPs is selectively achieved by laser absorption and the induced heat while the protective layer of the AgNPs, which aids dispersion of the particles in a solvent, dissociates [30]. In addition, the adhesion between the sintered AgNPs and substrate is increased. Fig. 6b shows the SEM images of as-coated AgNPs and laser-irradiated AgNPs. The morphology change induced by the laser irradiation suggests successful sintering.

Various patterns of conductive AgNP film can be easily obtained via programmed laser scanning because unaffected AgNPs are selectively washed out by water or alcohols. However, the adhesion between Ag and Si achievable via the laser sintering was not strong enough, and part of the patterned AgNP film was sometimes delaminated by washing with water. In our study, the poor adhesion was mitigated by placing a thin PI film (thickness: 5 μm, see Figure S8) at the interface mediating between the AgNP layer and Si surface, as described in section 2.3. PI was selected because it is a representative heat-resistive polymer that is intact at the sintering temperature of the AgNPs (~150 °C) [32] and the maximum temperature of the patterned heater (~240 °C).

The shape and dimensions of the serpentine heater pattern are shown in Fig. 6c and S2. The rectangular area enclosing the heater pattern was set to 10 mm × 10 mm, corresponding to that of the above microchannels; their X-Y positions were also matched with only the Z positions shifted by the wafer thickness. The electrical resistance of the heater element was ~ 46 Ω.

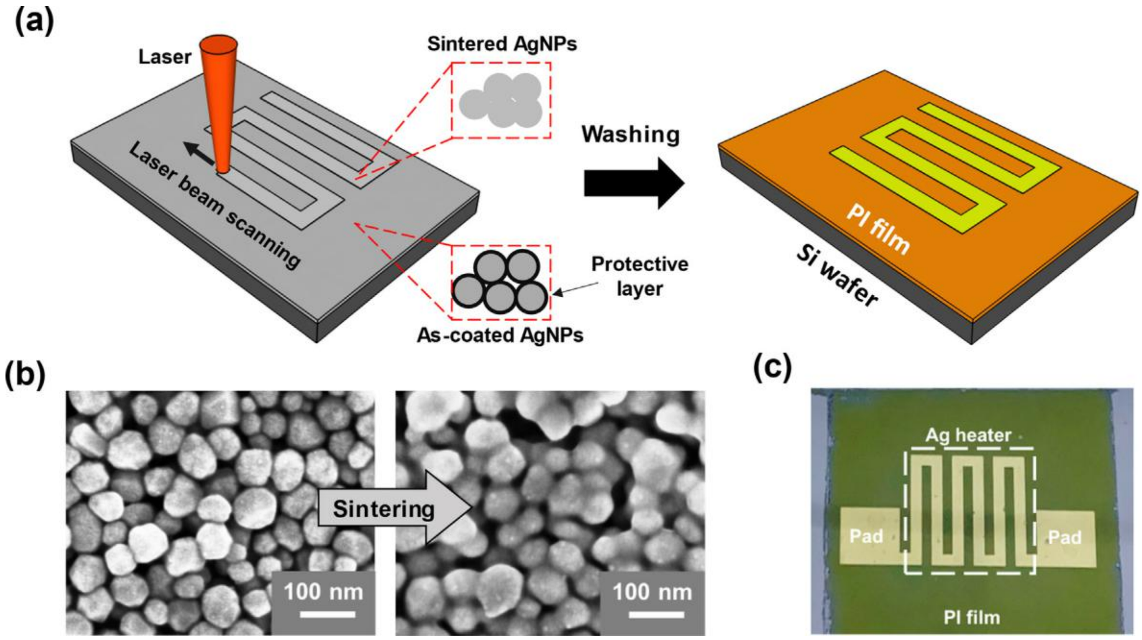

Fig. 6. (a) Schematic of laser sintering process. (b) FE-SEM images of unsintered and sintered AgNPs. (c) Digital image of Ag serpentine heater on PI film (each pad size: 5 mm × 5 mm).

3.2. Application in boiling heat transfer

The boiling heat transfer performance of the fabricated microchannel was evaluated by flowing liquid water through the microchannel heated by the on-chip micro-heater placed beneath the device. Fig. 7 shows a schematic diagram of the testing setup. Tubing (inner diameter: 2 mm) and tube fittings were connected to the inlet and outlet holes of the welded cover plate by using high-temperature resistant epoxy resin. DI water was injected into the microchannel at ambient temperature (~20 °C) at different mass flow rates using a syringe pump (SPLab01, SHENCHEN Co.). The on-chip heater was connected to a direct current power supply (6030A, Hewlett-Packard), and the heat flux was controlled by adjusting the voltage. The on-chip heater was coated with a high-emissivity black paint (ε = 0.93), and its surface temperature was monitored using an IR thermal imaging camera (FLIR A655sc; FLIR Systems, Inc.). Two pressure sensors (TruStability SSC Series, HONEYWELL Co.) were used to measure the pressure difference between the fluid inlet and outlet. The heater temperature, inlet/outlet pressures, and applied voltage/current data were recorded after a steady state was reached, where data fluctuations remained within 2 °C/min for temperature. The heater voltage was increased initially in steps of 5 V, but the step was reduced to 2 V after the onset of boiling. This process was repeated until CHF appeared.

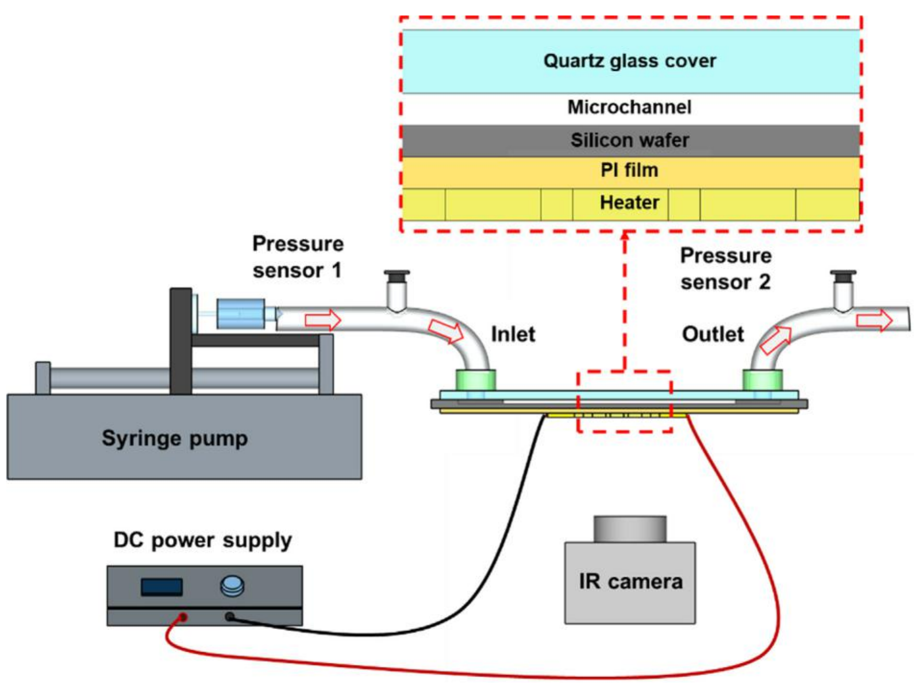

Fig. 7. Experimental schematic of flow boiling experiment.

The uncertainties of mass flow rate from the syringe pump and pressure from the two pressure sensors are ± 0.3 % and ± 0.25 %, respectively. A voltage divider was applied to the power supply for overvoltage protection to the data acquisition system (Ni-9174 and NI-9220, National Instruments). The power supply has an uncertainty of ± 0.3 W. The voltage divider consisted of two resistors with resistances of 47 kΩ ± 0.1 % and 3 kΩ ± 0.1 %, respectively, and a shunt resistor of 0.05 Ω ± 0.5 %. *T*-type thermocouples used for the fluid temperatures have accuracies of ± 1 °C, while the IR camera for the heated surface has an accuracy of ± 30 mK uncertainty with 0.4 % emissivity calibration. The details of emissivity calibration are found in our previous report [43]. The accumulated uncertainties are ± 14.6 %, ±1.4 %, ±2.9 %, and ± 3.2 % for pressure difference, heat flux, temperature, and heat transfer coefficient, respectively.

The temperature of the microchannel surface was calculated by assuming one-dimensional heat transfer:

$$T_s = T_h - q''_{eff}\left(\frac{w_{PI}}{k_{PI}} + \frac{w_{si}}{k_{si}}\right) \quad (1)$$

where T_s is the surface temperature of the Si wafer, T_h is the temperature of the heater, q''_{eff} is the heat flux, w_{PI} and k_{PI} are the thickness and thermal conductivity of the imidized PI film, and w_{Si} and k_{Si} are the thickness and thermal conductivity of the Si wafer, respectively. The pressure difference between the inlet and outlet (ΔP) is.

$$\Delta P = P_1 - P_2 \quad (2)$$

where P_1 and P_2 are the inlet and outlet pressures, respectively. Considering the heat loss caused by natural convection at the bottom of the Si substrate, the effective heat flux (q''_{eff}) is calculated as:

$$q''_{eff} = q'' - q''_{heat\ loss} \quad (3)$$

where q'' is the total heat flux of the heater and $q''_{heat\ loss}$ is the heat loss by the natural convection between the Si wafer substrate and the ambient (room temperature: 20 °C). In the calculation of $q''_{heat\ loss}$, the natural convective heat transfer coefficient (h) was assumed to be 5 W/(m^{2}K) [44]. The heat loss was calibrated by considering natural convection over the heated area. Based on our previous studies that adopted similar heater configurations, natural convective heat transfer coefficient over the heated area is estimated to be ~ 5 W/(m^{2}K). The surface of the test sample except the opening for IR measurement was covered with an insulating acrylic plate which has very low thermal conductivity, and the covered area was assumed to be fully insulated. Based on this calculation, the total heat loss by the natural convection is ~ 1 % at the maximum heat flux adopted in this study.

The saturation pressure (P_{sat}) in the middle of the microchannel is calculated as follows [45]:

$$P_{sat} = P_1 - \frac{\Delta P}{2} \quad (4)$$

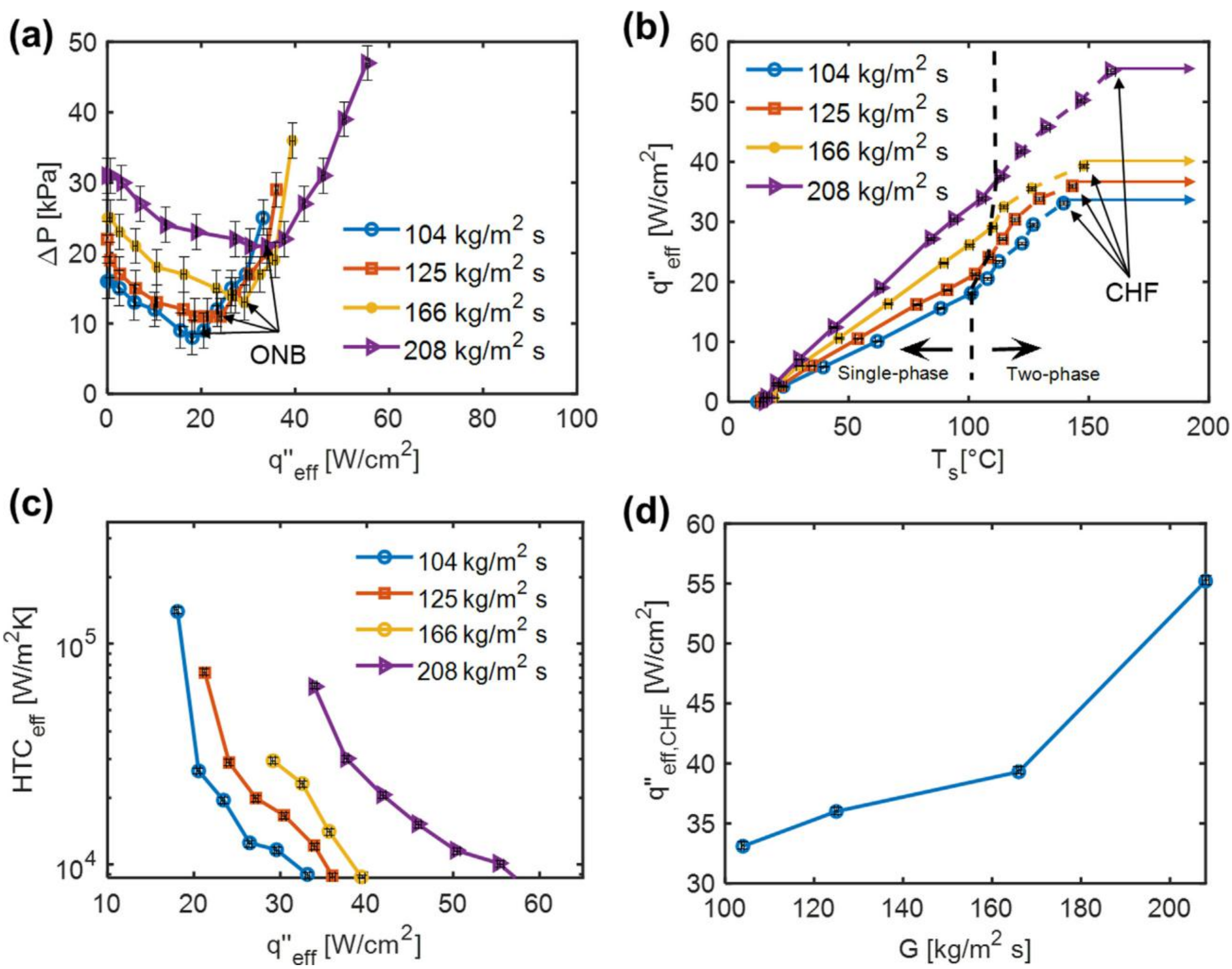

Fig. 8. Change in (a) pressure drop with effective heat flux at the mass flux of 104, 125, 166, and 208 kg/m^{2}s. (b) Boiling heat transfer performance for laser fabricated Si microchannel heat sink at different mass fluxes. Change in (c) effective heat transfer coefficient at different mass fluxes. Change in(d) effective critical heat flux with mass flux (G).

Effective boiling heat transfer coefficient (HTC_{eff}) is defined as:

$$HTC_{eff} = q''_{eff}/(T_s - T_{sat}) \quad (5)$$

The saturation temperature (T_{sat}) is thermodynamically determined from the local pressure.

The ONB (onset of nucleate boiling) point was recognized as a momentary rise in pressure drop, obtained from the minimum point of the pressure drop curve (Fig. 8a). With the increase of mass flux (G), the ONB temperature also gradually increased, and the ONB temperatures were 101.6, 108, 110, and 113 °C for 104, 125, 166, and 208 kg/m^{2}s, respectively. The ONB occurred at increased heat flux as the mass flux increased. CHF is the limited heat flux primarily caused by the local dry-out on the channel wall, resulting in an abrupt rise in temperature, detrimental to most temperature-sensitive devices [39]. However, as mentioned previously, the laser-engraved channel exhibited a hydrophilic nature with the capillary structure. As a result, the partially dry-out surface can be quickly replenished with water, maintaining the efficient boiling heat transfer. When investigated by SEM, the Si microchannel used in the above tests did not show any distinct change in structural characteristics (Figure S9), suggesting that the microchannels are quite stable in the examined flow and temperature conditions.

The maximum pressure drop was found to be 25, 29, 36, and 47 kPa at CHF points for 104, 125, 166, and 208 kg/m^{2}s, respectively. Fig. 8b shows the boiling heat transfer performance of the microchannel heat sink obtained at the different mass fluxes, revealing increased CHF with increasing mass flux. Fig. 8c shows the calculated heat transfer coefficient (HTC). For heat fluxes between ONB and CHF points, the average HTC was calculated to be 16.5 kW/m^2 K. Fig. 8d shows that CHF was 33.1, 36, 39, and 55.2 W/cm^2 for the mass fluxes of 104, 125, 166, and 208 kg/m^{2}s, respectively. Sitar et al. reported the boiling heat transfer performance of the device-level microchannels that was fabricated by dry-etching and additional laser structuring [46]. For 208 kg/m^{2}s, the CHF of our device (55.2 W/cm^2) was approximately 60 % higher than that of their device (33.6 W/cm^2 at 208 kg/m^{2}s), whereas they used a dilute butanol (6 wt%) in water for coolant.

4. Conclusions

In summary, we have developed an all-laser fabrication technique where lasers are comprehensively applied to major steps for fabricating fluidic devices with microchannels. A Si substrate was prepared by precisely cutting a Si wafer using a laser, and microchannels were engraved on the Si substrate. Inlet and outlet holes were laser drilled into a quartz glass cover, and the cover was welded with the Si substrate using a laser for packaging. A serpentine micro-heater film was patterned onto the bottom surface of the Si substrate via laser-induced sintering of AgNP film. All fabrication processes were performed under ambient conditions. Rapid programmable laser scanning especially enabled maskless patterning of microstructures such as microchannels and serpentine micro-heaters, remarkably shortening the fabrication time. The entire fabrication could be completed effectively within two hours.

A microchannel heat sink was fabricated based on the all-laser method, and its performance was evaluated. A highly hydrophilic channel wall was produced in the laser engraving of microchannels because of surface oxidation and the generation of complex capillary structures by laser ablation. This structure significantly improved flow boiling heat transfer when a water flow was introduced to the device. The flow boiling experiment revealed that the microchannel heat sink dissipated $\sim$ 55 W/cm^2 of heat at the mass flux of 208 kg/m^{2}s. We expect the heat transfer performance to be further improved by optimizing microchannel geometry, which will be investigated in future studies.

Conflict of Interest

The authors have no competing financial interest to declare.

Data availability

Data will be made available on request.

Declaration of Competing Interest

The authors declare that they have no known competing financial interests or personal relationships that could have appeared to influence the work reported in this paper.

Acknowledgments

This work was supported by Samsung Research Funding & Incubation Center of Samsung Electronics under Project Number SRFC-TA1903-06, and by the Korea Institute of Energy Technology Evaluation and Planning (KETEP) and the Ministry of Trade, Industry & Energy (MOTIE) of the Republic of Korea (No. 20214000000280).

Data availability

The raw/processed data required to reproduce these findings cannot be shared at this time as the data also forms part of an ongoing study.

Appendix A. Supplementary data

Supplementary data to this article can be found online at https://doi.org/10.1016/j.matdes.2022.110968.

References

[1] D. Zhuang, Y. Yang, G. Ding, X. Du, Z. Hu, Optimization of microchannel heat sink with rhombus fractal-like units for electronic chip cooling, Int. J. Refrig 116 (2020) 108–118.
[2] N.H. Naqiuddin, L.H. Saw, M.C. Yew, F. Yusof, T.C. Ng, M.K. Yew, Overview of micro-channel design for high heat flux application, Renew. Sustain. Energy Rev. 82 (2018) 901–914.
[3] A.-E.-M.-A. Harb, A. Radwan, K. Elsayed, M. Sedrak, M. Ahmed, Influence of varying the Ethylene-Vinyl Acetate layer thicknesses on the performance of a polycrystalline silicon solar cell integrated with a microchannel heat sink, Sol. Energy 195 (2020) 592–609.
[4] C.T. Lu, C. Pan, Convective boiling in a parallel microchannel heat sink with a diverging cross section and artificial nucleation sites, Exp. Therm Fluid Sci. 35 (2011) 810–815.
[5] Y. Jia, G. Xia, L. Zong, D. Ma, Y. Tang, A comparative study of experimental flow boiling heat transfer and pressure drop characteristics in porous-wall microchannel heat sink, Int. J. Heat Mass Transf. 127 (2018) 818–833.
[6] K.N. Ramesh, T.K. Sharma, G.A.P. Rao, Latest Advancements in Heat Transfer Enhancement in the Micro-channel Heat Sinks: A Review, Arch. Comput. Methods Eng. 28 (2021) 3135–3165.
[7] S. Zheng, Z. Feng, Q. Lin, Z. Hu, Y. Lan, F. Guo, K. Huang, F. Yu, Numerical investigation on thermal-hydraulic characteristics in a mini-channel with trapezoidal cross-section longitudinal vortex generators, Appl. Therm. Eng. 118004 (2021).
[8] D.J. Harrison, K. Fluri, K. Seiler, Z. Fan, C.S. Effenhauser, A. Manz, Micromachining a miniaturized capillary electrophoresis-based chemical analysis system on a chip, Science 261 (1993) 895–897.
[9] S.C. Jacobson, R. Hergenröder, L.B. Koutny, J.M. Ramsey, Open channel electrochromatography on a microchip, Anal. Chem. 66 (1994) 2369–2373.
[10] S.C. Jacobson, A.W. Moore, J.M. Ramsey, Fused quartz substrates for microchip electrophoresis, Anal. Chem. 67 (1995) 2059–2063.
[11] P. Mao, J. Han, Massively-parallel ultra-high-aspect-ratio nanochannels as mesoporous membranes, Lab Chip 9 (2009) 586–591.
[12] D. Jung, H. Lee, D. Kong, E. Cho, K.W. Jung, C.R. Kharangate, M. Iyengar, C. Malone, M. Asheghi, K.E. Goodson, H. Lee, Thermal design and management of micro-pin fin heat sinks for energy-efficient three-dimensional stacked integrated circuits, Int. J. Heat Mass Transf. 175 (2021).

[13] S.M. Scott, Z. Ali, Fabrication Methods for Microfluidic Devices: An Overview, Micromachines 12 (2021) 319.
[14] A. Grosse, M. Grewe, H. Fouckhardt, Deep wet etching of fused silica glass for hollow capillary optical leaky waveguides in microfluidic devices, J. Micromech. Microeng. 11 (2001) 257.
[15] E. Brousseau, S.S. Dimov, D.T. Pham, Some recent advances in multi-material micro-and nano-manufacturing, The International Journal of Advanced Manufacturing Technology 47 (2010) 161–180.
[16] R. Chantiwas, M.L. Hupert, S.R. Pullagurla, S. Balamurugan, J. Tamarit-López, S. Park, P. Datta, J. Goettert, Y.K. Cho, S.A. Soper, Simple replication methods for producing nanoslits in thermoplastics and the transport dynamics of double-stranded DNA through these slits, Lab Chip 10 (2010) 3255–3264.
[17] H. Shadpour, S.A. Soper, Two-dimensional electrophoretic separation of proteins using poly(methyl methacrylate) microchips, Anal. Chem. 78 (2006) 3519–3527.
[18] E. Gandarias, S. Dimov, D.T. Pham, A. Ivanov, K. Popov, R. Lizarralde, P. Arrazola, New methods for tool failure detection in micromilling, Proceedings of the Institution of Mechanical Engineers, Part B: Journal of Engineering Manufacture 220 (2006) 137–144.
[19] X. Cheng, Z. Wang, K. Nakamoto, K. Yamazaki, A study on the micro tooling for micro/nano milling, The International Journal of Advanced Manufacturing Technology 53 (2010) 523–533.
[20] B. Kirsch, M. Bohley, P.A. Arrabiyeh, J.C. Aurich, Application of Ultra-Small Micro Grinding and Micro Milling Tools: Possibilities and Limitations, Micromachines 8 (2017) 261.
[21] T.H.R. Crawford, A. Borowiec, H.K. Haugen, Femtosecond laser micromachining of grooves in silicon with 800 nm pulses, Appl. Phys. A 80 (2005) 1717–1724.
[22] S. Hopman, K. Mayer, A. Fell, M. Mesec, F. Granek, Laser cutting of silicon with the liquid jet guided laser using achlorine-containing jet media, Applied Physics A: Materials Science Processing 102 (2010) 621–627.
[23] D.H. Kam, J. Mazumder, Three-dimensional biomimetic microchannel network by laser direct writing, J. Laser Appl. 20 (2008) 185–191.
[24] D. Kam, L. Shah, J. Mazumder, Femtosecond laser machining of multi-depth microchannel networks onto silicon, J. Micromech. Microeng. 21 (2011) 045027.
[25] D.H. Kam, J. Kim, J. Mazumder, Near-IR nanosecond laser direct writing of multi-depth microchannel branching networks on silicon, J. Manuf. Processes 35 (2018) 99–106.
[26] V. Tangwarodomnukun, S. Mekloy, Temperature field modeling and cut formation in laser micromachining of silicon in ice layer, J. Mater. Process. Technol. 271 (2019) 202–213.
[27] G. Cummins, H. Lin, A. Walton, Measurement and optimisation of bond strength for anodic bonding of glass to dielectric thin films, 2008 IEEE International Conference on Microelectronic Test Structures, 2008, pp. 111–116.
[28] M. Esashi, Wafer level packaging of MEMS, J. Micromech. Microeng. 18 (2008) 073001.
[29] W.P. Eaton, J.H. Smith, Micromachined pressure sensors: review and recent developments, Smart Mater. Struct. 6 (1997) 530.
[30] P.T. Nguyen, J. Jang, Y. Lee, S.T. Choi, J.B. In, Laser-assisted fabrication of flexible monofilament fiber supercapacitors, J. Mater. Chem. A 9 (2021) 4841–4850.
[31] H. Choi, P.T. Nguyen, C.V. Tran, J.B. In, Micro-patterned metal current collectors for high aspect ratio flexible graphene supercapacitors, Appl. Surf. Sci. 510 (2020).
[32] J. Jang, H. Zhou, J. Lee, H. Kim, J.B. In, Heat Scanning for the Fabrication of Conductive Fibers, Polymers 13 (2021) 1405.
[33] V. Mohammad, S.M. Farhad, R.N. Elaheh, S.A. Mehdi, M. Shokouhimehr, Heat transfer and pressure drop in a ZrB2 microchannel heat sink: A numerical approach, Ceram. Int. 46 (2020) 1730–1735.
[34] S.M. Bagheri, M. Vajdi, F.S. Moghanlou, M. Sakkaki, M. Mohammadi, M. Shokouhimehr, M.S. Asl, Numerical modeling of heat transfer during spark plasma sintering of titanium carbide, Ceram. Int. 46 (2020) 7615–7624.
[35] K. Vaferi, S. Nekahi, M. Vajdi, F.S. Moghanlou, M. Shokouhimehr, A. Motallebzadeh, J.J. Sha, M.S. Asl, Heat transfer, thermal stress and failure analyses in a TiB2 gas turbine stator blade, Ceram. Int. 45 (2019) 19331–19339.
[36] C.J. Yang, X.B. Jing, F.J. Wang, O.R.N. Ehmann, Y.L. Tian, Z.H. Pu, Fabrication of controllable wettability of crystalline silicon surfaces by laser surface texturing and silanization, Appl. Surf. Sci. 497 (2019).
[37] F. Hong, P. Cheng, H. Wu, Z. Sun, Evaporation/boiling heat transfer on capillary feed copper particle sintered porous wick at reduced pressure, Int. J. Heat Mass Transf. 63 (2013) 389–400.
[38] S. Fan, L. Jiao, K. Wang, F. Duan, Pool boiling heat transfer of saturated water on rough surfaces with the effect of roughening techniques, Int. J. Heat Mass Transf. 159 (2020) 120054.
[39] N. Tran, U. Sajjad, R. Lin, C.-C. Wang, Effects of surface inclination and type of surface roughness on the nucleate boiling heat transfer performance of HFE-7200 dielectric fluid, Int. J. Heat Mass Transf. 147 (2020) 119015.
[40] W. Deng, S. Ahmad, H.Q. Liu, J.T. Chen, J.Y. Zhao, Improving boiling heat transfer with hydrophilic/hydrophobic patterned flat surface: A molecular dynamics study, Int. J. Heat Mass Transf. 182 (2022).
[41] J.B. In, H.J. Kwon, J.H. Yoo, F.I. Allen, A.M. Minor, C.P. Grigoropoulos, Laser welding of vertically aligned carbon nanotube arrays on polymer workpieces, Carbon 115 (2017) 688–693.
[42] H. Choi, P.T. Nguyen, J.B. In, Laser transmission welding and surface modification of graphene film for flexible supercapacitor applications, Appl. Surf. Sci. 483 (2019) 481–488.
[43] D. Kong, M. Kang, K.Y. Kim, J. Jang, J. Cho, J.B. In, H. Lee, Hierarchically Structured Laser-Induced Graphene for Enhanced Boiling on Flexible Substrates, ACS Appl. Mater. Interfaces 12 (2020) 37784–37792.
[44] D. Kong, K.W. Jung, S. Jung, D. Jung, J. Schaadt, M. Lyengar, C. Malone, C.R. Kharangate, M. Asheghi, K.E. Goodson, H. Lee, Single-phase thermal and hydraulic performance of embedded silicon micro-pin fin heat sinks using R245fa, Int. J. Heat Mass Transf. 141 (2019) 145–155.
[45] G. Huang, W. Li, J. Ma, C. Ren, C. Li, High-frequency alternating nucleate boiling of water enabled by microslot arrays in microchannels, Int. J. Heat Mass Transf. 150 (2020) 119271.
[46] A. Sitar, M. Crivellari, J. Schille, S. Mauersberger, U. Löschner, I. Golobič, Improved Boiling Heat Transfer in Dry Etched Microchannels With Laser Structured Surfaces, in: International Conference on Nanochannels, Microchannels, and Minichannels, American Society of Mechanical Engineers, 2018, pp. V001T002A015.